Experimental investigation of the flame structure of dilute sprays issuing into a hot and low-oxygen coflow

Douglas B. Proud[a,*], Michael J. Evans[a,b], Paul R. Medwell[a], Qing N. Chan[c]

[a] *School of Mechanical Engineering, The University of Adelaide, Adelaide, SA 5005, Australia*
[b] *University of South Australia, Mawson Lakes, SA 5095, Australia*
[c] *School of Mechanical and Manufacturing Engineering, University of New South Wales, Sydney, NSW 2052, Australia*

Abstract

The combustion of liquid fuels in a hot and low-oxygen environment is commonly encountered in a range of practical situations. To enable investigation of the fundamental combustion processes relating to such applications, liquid fuels were injected into the reaction zone as dilute sprays in this study. Droplets of ethanol, *n*-heptane, and *n*-heptane/toluene blends were produced via an ultrasonic nebuliser, and were carried by air through a central jet to a hot coflow of combustion products. The resulting flames were then analysed using four simultaneous laser diagnostic techniques. Planar laser-induced fluorescence (PLIF) was implemented to perform imaging of key intermediate species, including hydroxyl (OH) and formaldehyde (CH_2O), while the Mie scattering technique was used to detect the location of droplets. The sooting behaviour of these flames was also investigated, via the laser-induced incandescence (LII) technique. The existence of distinct inner and outer reaction zones is a key feature of all of the flames studied, and this "double flame structure" was found to be related to partial premixing of air and fuel, as well as penetration of droplets into the inner reaction zone. A change in the stabilisation of the inner flame front was observed with variations in fuel type, with a greater likelihood of ignition kernels in the case of the *n*-heptane and *n*-heptane/toluene flames, whereas the

*Corresponding author. E-mail: douglas.proud@adelaide.edu.au

equivalent ethanol flame displays a bifurcation structure. Variations in the jet Reynolds number and liquid fuel loading were also found to have a notable impact on the distribution and evaporation of droplets, which was in turn found to affect the formation of the double flame structure. Due to the complex coupling between turbulence, chemistry and droplet evaporation in these flames, the accurate prediction of such results *a priori* is not within the limits of current modelling capabilities. These findings provide a valuable insight to enable future advancements in spray combustion modelling and the design of practical combustion devices.
Keywords: Spray combustion, Mild combustion, Laser diagnostics, Autoignition, Flame stabilisation

1. Introduction

The combustion of liquid fuels accounts for approximately 35% of the primary energy consumption in the modern world. Liquid fuels are typically injected in the form of a spray, to accelerate the evaporation and subsequent combustion of the fuel [1, 2]. Despite the widespread use of liquid sprays in combustion devices such as gas turbines and reciprocating engines, current understanding of the behaviour of liquid spray flames remains incomplete, particularly in regards to the development and validation of accurate and efficient computational models [3]. This is largely due to the complex nature of the coupled interactions between spray break-up and evaporation, combustion chemistry, and turbulence.

In broad terms, a spray—or a certain region of a spray—can be classified as being either "dense" or "dilute". For classification purposes, a spray can be considered dilute when the liquid loading is less than approximately 1% by volume and the interactions between droplets are negligible [4, 5]. In practical situations, liquid fuels are typically injected as a dense spray, which subsequently breaks-up and evaporates, forming a dilute spray [6]. In order to focus on the fundamental combustion processes relating to fuel droplets in an experimental

context, a dilute spray can be directly formed and transported into the reaction zone via a carrier gas. Detailed measurements of reactive scalars and droplet fields have previously been obtained for dilute sprays [5, 7], as part of the International Workshop on Turbulent Combustion of Sprays (TCS), which is aimed at providing insight for the development of practical models. Despite this, there still remains a lack of detailed data for certain types of flames, particularly in conditions related to sequential gas turbines and engines using exhaust gas recirculation (EGR) [8, 9].

Liquid sprays reacting in a high-temperature, low-oxygen environment are commonly encountered in combustion devices which use techniques such as EGR and mild combustion [10, 11]. These methods enable improvements in efficiency and combustion stability, along with emissions reductions [12, 13]. The term "mild" has been used here to encapsulate the features of moderate or intense low-oxygen dilution combustion, a particular regime with very high dilution by hot combustion products, characterised by distributed reaction zones, lower peak temperatures, and significant reductions in emissions of NO_x, CO and soot [14].

The behaviour of flames under mild combustion conditions is significantly different to that of conventional flames [15]. The reduced concentration of O_2 results in longer chemical time-scales [16], and a change in the stabilisation mechanism of visually lifted flames has been observed [17]. To examine the fundamental physical and chemical processes which govern flames in this regime, and to facilitate the development of numerical models, most studies have been focussed on relatively simple, gaseous fuels. Many of these fundamental experimental studies have been carried out using a type of burner commonly referred to as a "jet in hot cross-/co-flow" (JHC) configuration [18, 19, 20, 21], which allows the fuel composition and flow rate to be varied independently of the temperature and O_2 concentration of the oxidant stream, and also facilitates the use of laser diagnostic techniques.

The behaviour of liquid fuels in the mild combustion regime has also been investigated. To study the chemical effects in isolation, a series of experiments

were performed with a JHC configuration using prevaporised fuels, including ethanol and blends of n-heptane/toluene [22, 23]. A change in flame structure was observed when the O_2 concentration was increased from 3% to 9%, suggesting a shift away from the mild combustion regime [22]. An analysis of reaction fluxes indicated a fundamental change in chemical kinetics, with greater sensitivity to fuel-specific reactions in the 9% O_2 case [22]. A significant increase in soot formation with addition of toluene to the fuel was also observed, which was found to have a notable impact on the flame temperature [23]. Measurements of the gas, droplet and temperature fields were attained for the "Delft spray in hot coflow" (DSHC) flames [24], which uses a pressure-swirl atomiser to generate droplets. These experiments highlighted a change in spray break-up and evaporation processes when comparing spray flames in a coflow of air versus a hot-diluted coflow. This change was found to have a large impact on the flame structure and temperature field, with the rapid spray break-up and vaporisation in the hot coflow leading to a reduction in peak temperatures and a more uniform distribution. The temperature profiles also indicated the presence of separate inner and outer reaction zones for both coflow conditions, although this was most obvious in the case of an air coflow.

The existence of multiple reaction zones is a commonly observed feature of spray flames. In a simplified numerical analysis of a counterflow spray configuration, two distinct flame zones were predicted to occur under certain conditions; this was attributed to the flame exhibiting both premixed and diffusion-like characteristics, with a merging of the two zones at high strain rates [25]. This "double flame" structure has been observed in other experiments involving sprays [26, 27], and has also been reproduced via large-eddy simulation (LES) [28]. This latter study found that there were actually up to four distinct reaction regions in the case of an air coflow, despite the associated experimental results suggesting a double flame structure [28]. Additionally, the formation of these multi-flame structures was found to be very sensitive to the relative evaporative and chemical time-scales, highlighting the complexity involved in the modelling of dual-phase combustion [28]. The flame structure has also been investigated

using a RANS approach, where bifurcating flame fronts were found to occur at lower coflow temperatures [29]. Although the presence of multi-flame structures (i.e. flames with distinct reaction zones) has been observed both experimentally and numerically, the underlying mechanisms which lead to these structures requires further investigation to enable robust and efficient numerical models to be developed.

To bridge the gap between the understanding of gaseous fuels undergoing autoignition in a hot coflow and the experiments performed with piloted dilute sprays [30], a dilute spray burner for studying spray flames in a hot and low-oxygen coflow was developed [31]. Imaging of the hydroxyl (OH) radical was performed to study the formation of ignition kernels, and it was found that autoignition occurs in a relatively gradual manner and over a larger range of distances compared with gaseous flames [31]. In a separate study with the same burner configuration [32], a double flame structure was observed when air was used as the carrier gas, which was hypothesised to be a result of vaporised liquid mixing with air to produce localised, ignitable mixtures. Another important feature of these flames was the presence of formaldehyde (CH_2O) prior to OH formation, highlighting the importance of this radical in the autoignition process. Heat release rate was also examined qualitatively in this study, using the product $[OH]\times[CH_2O]$ as a marker [32]. A limitation of these studies [31, 32], and indeed all of those involving sprays in hot and vitiated coflows, is the lack of simultaneous imaging of both droplets and chemical species, which has been performed in previous studies involving dilute spray burners [5, 33].

The present study aims to extend the understanding of spray combustion in a hot and low-oxygen environment, using a dilute spray burner in a JHC configuration. The stabilisation mechanisms and near-field flame structure are of particular focus, along with the distribution of fuel droplets and the effect that this has on the flame further downstream. The results presented correspond to constant coflow conditions, while a range of jet boundary conditions and fuel compositions are investigated. A series of simultaneous laser diagnostic techniques are implemented, providing a unique insight into the structure of

these flames and facilitating future development of spray combustion models. Planar laser-induced fluorescence (PLIF) is performed to allow imaging of the hydroxyl (OH) and formaldehyde (CH_2O) radicals, while the Mie scattering technique is used to capture the location of droplets. Additionally, laser-induced incandescence (LII) is performed to measure the soot volume fraction, and how this varies with fuel composition.

2. Methodology

2.1. Spray burner description

The spray burner used in this study shares several features with well-studied JHC and dilute spray burners, which have been used to study both piloted and autoignitive flames [18, 22, 30, 31, 32, 34]. The burner and laser diagnostics configuration is equivalent to that which has previously been used to study hydrogen flames with toluene addition, albeit without a hot coflow [34]. A schematic of this burner is shown in Figure 1. Fuel droplets with minimal initial momentum are generated using an ultrasonic nebuliser, with an estimated Sauter mean droplet diameter (SMD) of 30 µm at the nebuliser head. This estimate is based on data from the manufacturer (Sonotek), in conjunction with a commonly used correlation for the diameter of droplets (d_{SMD}) generated via ultrasonic nebulisation [35]:

$$d_{SMD} = c\left(\frac{8\pi\sigma}{\rho f^2}\right)^{1/3}, \tag{1}$$

where c is an empirically derived constant which depends on the specific nebuliser used, f is the vibrational frequency of the nebuliser, and σ and ρ are the surface tension and density of the liquid being used, respectively. The viscosity (μ) of the liquid is also known to have an effect on the atomisation process, although previous findings suggest that this effect only becomes significant for $\mu > 10$ mPa·s [36], which is an order of magnitude greater than the viscosity of the liquids used in this investigation.

The nebuliser is located inside a brass housing which has a smooth, tapered exterior, which is in turn contained within a smooth, stainless steel internal contraction. Carrier air flows around the outside of the brass housing, to collect the droplets at the nebulising surface, which is flush with the top of the brass housing. These droplets are then carried by air to the jet exit, which is located approximately 270 mm downstream of the nebuliser. The jet diameter (D) is 20 mm (ID), while the surrounding coflow diameter is 110 mm. The hot coflow is produced via the lean premixed combustion of natural gas and air, stabilised on a porous bed burner positioned 10 mm upstream of the jet exit plane. The porous bed has a depth of 90 mm, containing flint clay with a maximum flint size of 5 mm. The coflow conditions were held constant, with a temperature of 1690 K and a calculated O_2 concentration of 7.5% (by volume). These coflow conditions were selected to enable comparisons with previous studies involving prevaporised fuels [23, 37]. Air at room temperature issues from a 130 mm (OD) annulus surrounding the coflow with a velocity of 0.4 m/s, to reduce mixing of the jet and coflow with the surrounding quiescent air.

Four different liquid fuel compositions were used in this study; namely ethanol, n-heptane, and 3:1 and 1:1 blends of n-heptane and toluene (n-heptane:toluene, by liquid volume). These were selected to allow the effects of fuel chemistry to be analysed, particularly in regards to soot formation, as well as the potential for comparison against previous results. Additionally, the variation in physical properties of the different liquids is considered when comparing the flame cases. For the ethanol flames, the flow rates of both the carrier gas (air) and the liquid fuel were also independently varied. These correspond to changes in the jet Reynolds number (Re_{jet}) and the liquid fuel loading ($\dot{m}_f$), respectively, noting that the changes in $\dot{m}_f$ have a negligible impact on the bulk volumetric flow rate through the jet.

The operating conditions and the name of their associated flame cases are listed in Table 1, along with the values of equivalence ratio for each case, based on the total mass of fuel and carrier air. The cases are named according to the type of fuel used (E $\equiv$ Ethanol, H $\equiv$ n-heptane, T $\equiv$ Toluene), the liquid fuel

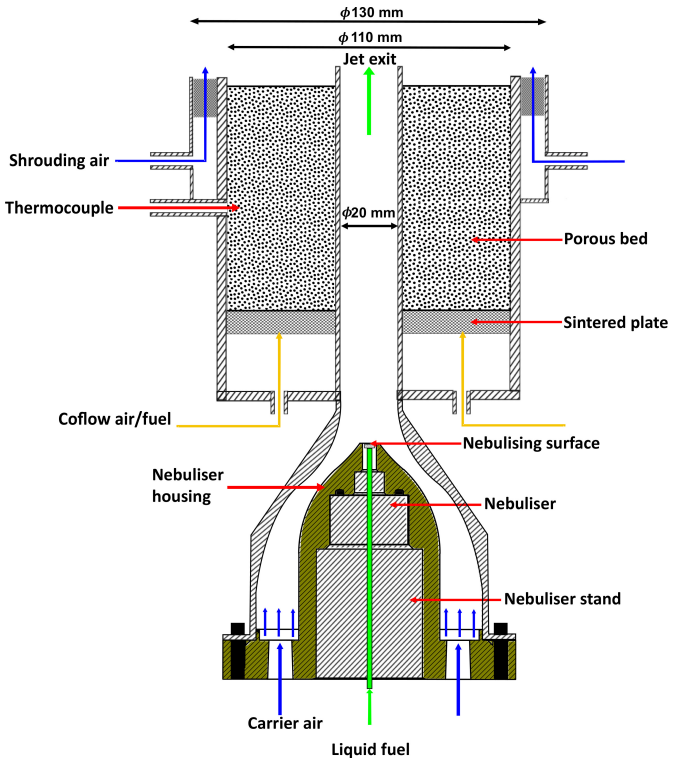

Figure 1: Schematic cross-section of spray burner and nebuliser (not to scale).

flow rate, and the jet Reynolds number. For example, case "E21-5" refers to an ethanol flame with 0.21 g/s liquid fuel loading and Reynolds number of 5000. To differentiate between the 3:1 and 1:1 *n*-heptane/toluene blends, "HT" is used for the 3:1 blend, while "TH" is used for the 1:1 blend. The surface tension (σ), vapour pressure (P_v) and boiling point (T_b) of the pure liquid fuels used are shown in Table 2, in addition to the values of ρ and μ for all fuel compositions.

2.2. Diagnostic techniques

The optical diagnostics configuration used in this study was identical to that which was used in a previous study with a similar spray burner [34]. Simultaneous imaging of soot volume fraction, fuel droplets, hydroxyl radicals (OH) and formaldehyde (CH_2O) was achieved using four separate laser diagnostic techniques. Three Nd:YAG lasers and one Nd:YAG-pumped dye laser were used to

Table 1: Table of flame cases, indicating the fuel composition, fuel loading ($\dot{m}_f$), jet equivalence ratio (Φ_{jet}) and Reynolds number (Re_{jet}).

Case	Fuel composition	$\dot{m}_f$ [g/s]	Φ_{jet}	Re_{jet}
E15-5	Ethanol	0.15	0.95	5000
E21-5	Ethanol	0.21	1.3	5000
E27-5	Ethanol	0.27	1.7	5000
E21-3	Ethanol	0.21	2.2	3000
E21-6	Ethanol	0.21	1.1	6000
H21-5	*n*-heptane	0.21	2.2	5000
HT21-5	3:1 *n*-heptane:toluene	0.21	2.2	5000
TH21-5	1:1 *n*-heptane:toluene	0.21	2.1	5000

Table 2: Table of liquid fuel properties. All properties correspond to a pressure of 1 bar and temperature of 20 °C, with mixture properties calculated based on empirical correlations for binary mixtures [38, 39].

Fuel Composition	ρ [kg/m^3]	μ [mPa·s]	σ [mN/m]	P_v [kPa]	T_b [°C]
Ethanol	789	1.2	22.4	6.0	78.4
n-heptane	684	0.41	20.1	5.3	98.4
Toluene	867	0.59	28.5	2.9	110.6
3:1 *n*-heptane:toluene	728	0.44			
1:1 *n*-heptane:toluene	774	0.47			

produce vertical sheets of 10 Hz pulsed laser light of different wavelengths, each with a nominal height of 15 mm. The burner was traversed vertically through the laser sheet to measure different heights (x) in the flame, ranging from the jet exit plane to 112 mm downstream ($x/D = 5.6$). This range allows the near-field flame structure to be analysed, in terms of flame stabilisation and the existence of multiple reaction zones. For each diagnostic, sets of 255 images were captured for each flame case and measurement location, allowing both instantaneous and time-averaged analyses to be performed.

The frequency-doubled output of an Nd:YAG laser (532 nm) was used to

observe fuel droplets via the Mie scattering technique. The laser was operated with an energy of 0.5 mJ/pulse, and the scattered light was detected using a CCD camera through an f/5.6 lens with a 500 ns gate width. The lens was fitted with a bandpass filter centred at 532 nm with a FWHM of 10 nm and transmission $> 85\%$, to prevent interference from other signals.

Planar laser-induced fluorescence (PLIF) was used for imaging of both OH and CH_2O. For the OH-PLIF, a frequency-doubled dye laser was tuned to a wavelength of 282.927 nm to excite the $Q_1(6)$ transition of the OH radicals. The $Q_1(6)$ transition was selected due to its relatively low sensitivity to temperature fluctuations in the range of interest, and the fact that it provides a stronger signal in comparison to the $Q_1(7)$ transition. The output of the dye laser had a measured energy of approximately 1 mJ/pulse, and it was pumped by a frequency-doubled Nd:YAG laser. The resulting fluorescence of OH radicals was imaged using an ICCD camera operated with a gate width of 100 ns, with an f/3.5 UV lens. A 310 nm bandpass filter (10 nm FWHM, peak transmission $> 70\%$) was fitted to the UV lens.

For the CH_2O-PLIF, the third harmonic (355 nm) of an Nd:YAG laser was used, with a measured energy of 120 mJ/pulse. An ICCD camera (100 ns gate width) was used for CH_2O imaging, with a bandpass filter centred at 410 nm (10 nm FWHM, transmission $> 45\%$), along with an f/1.2 lens. It should be noted that UV excitation is known to cause broadband fluorescence of a range of carbonaceous species in a flame, including polyaromatic hydrocarbons (PAH). In most of the results presented, particularly for measurements made near the flame base, CH_2O is expected to dominate the signal, as has been observed in previous studies of similar flames stabilised via autoigntion [5]. However, since there is some interference, particularly for the *n*-heptane/toluene flames and in the downstream locations, the results presented in this paper refer to the signal detected from the 355 nm laser using the label of "UV" to account for this. This scalar measurement is indicative of precursor reactions, whether the collected signal is CH_2O or other species which fluoresce in the detected UV region.

Laser-induced incandescence (LII) was used to measure the soot volume

fraction (f_v), using the fundamental output (1064 nm) of an Nd:YAG laser with a fluence of 800 mJ/cm^2/pulse at the detection location. This ensures that the measurements correspond to the "plateau region", in which the LII signal is less sensitive to fluctuations in the laser power [40, 41, 42]. The incandescence from the soot particles was observed through an ICCD camera with an f/1.8 lens and a gate width of 100 ns. The camera was also fitted with a bandpass filter, with peak transmission of 45% at 430 nm and FWHM of 10 nm. In order to quantify the soot measurements, calibration was performed against extinction measurements in a premixed, laminar flame (ethylene-air, $\Phi = 2.4$) stabilised on a McKenna burner, similar to previous studies [23, 34, 43].

The timing of the lasers and cameras was controlled using a combination of delay/pulse generators, configured such that all laser pulses were within 400 ns of each other. The 1064 nm LII pulse occurred last, to avoid interference from the broadband incandescent radiation. It should be noted that despite the Mie scattering camera being operated with a gate width of 500 ns, such that there was overlap with the 1064 nm pulse, there was no appreciable interference from LII, due to the strength of the Mie scattering signal. Images were corrected for dark charge, vignetting, and any background signal present, and the OH-PLIF signals were also corrected to account for the variation in intensity of the laser sheet in the vertical direction. Images were spatially matched to sub-pixel accuracy, with a pixel size of $\sim$130 µm. A 3×3 median filter was applied to the raw PLIF and LII images to improve the signal-to-noise ratio, while the Mie scattering images were left unfiltered. Out-of-plane resolution (i.e. sheet thickness) has been estimated to be approximately 400 µm.

Additional processing of the Mie scattering images was performed in order to extract data related to the number of droplets and their spatial distributions. A counting algorithm based on the binarised Mie scattering images was implemented, to determine the number and location of droplets in each instantaneous image. A radial weighting was also applied, such that the droplet count is scaled relative to the distance from the centreline, to account for cylindrical integration of the planar measurements. This process was applied to a set of

255 images for each case, and these values were then averaged following the removal of any outliers, ensuring statistical convergence of the mean data. For $x/D < 3.0$, the uncertainty in these measurements ranges from 2–6%, while the uncertainty across all axial locations and flame cases is less than 10%. To analyse the droplet distributions with respect to the underlying flame structure, the UV-PLIF signal was used as a spatial threshold for the Mie scattering images, such that the droplets could be divided into those which occur inside the continuous CH_2O layer, and those which occur outside. In order to isolate the continuous structures in the UV-PLIF images, a combination of image processing techniques were implemented, following a similar method to that which has previously been used to detect primary particles in images of soot aggregates [44, 45, 46]. Specifically, the process involved dilation and erosion of the images, and the resulting structures were filtered by size and eccentricity. The division of the images into "inner" and "outer" regions is further discussed in context with the structure of the flames in Section 3.3.

Photographs of the flames were captured using a DSLR camera, with exposure times ranging from 30 s to 250 μs, although long exposures were not achievable for certain cases due to saturation. The photographs presented in this paper were all captured with an f-number of 16 and an ISO value of 100, with manual focus and white balance.

3. Results and discussion

3.1. Visual observations

Photographs of the eight different flames, corresponding to changes in fuel loading, Reynolds number and fuel composition, are shown in Figure 2. For the ethanol flames, the photographs shown have exposure times of 4 s, while the *n*-heptane and *n*-heptane/toluene flames have exposures of 0.5 s; these different exposures were required due to the differences in flame luminosities resulting from the increased soot loading of the *n*-heptane and *n*-heptane/toluene flames. All other camera settings were held constant for the different cases. The boxed

region in the images represents the the range of heights at which laser diagnostic data were collected in this study.

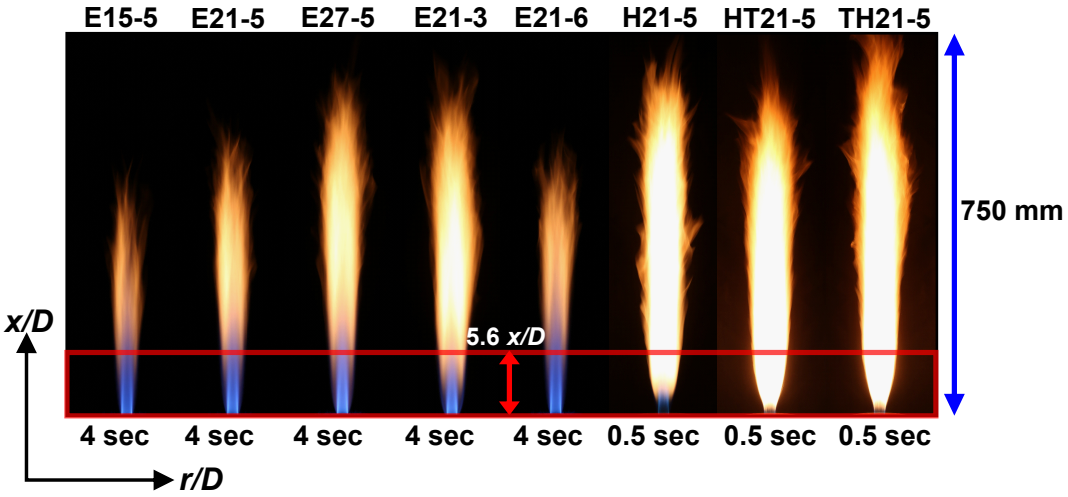

Figure 2: Flame photographs captured with a DSLR camera with exposure times as shown, with an f-number of 16 and ISO of 100.

The increase in luminosity for the *n*-heptane and *n*-heptane/toluene flames is clearly evident in the photographs (particularly taking the different exposures into account), which is attributed to higher levels of soot in these flames. Looking at the ethanol flames alone, there also appears to be an increase in luminosity with increasing fuel loading, and decreasing Re_{jet} (which also corresponds to increasing equivalence ratio). With the exception of the *n*-heptane/toluene flames (cases HT21-5 and TH21-5), a blue inner cone can also be observed at the base of the flames. A fainter blue region can be observed outside of the inner cone near the base of some of the flames (particularly the E21-3 flame), which transitions to a yellow/orange flame further downstream, suggesting a double flame structure. The near-field flame structure has a significant impact on the overall appearance of these flames—this is further discussed in Sections 3.4 and 3.5.

The photographs show noticeable changes in the visible flame length for the different cases. The first three images, looking from left-to-right, show a consistent increase in flame length with fuel loading. Since the flow rate of carrier

air is held constant for these cases (i.e. Re_{jet} is constant), Φ_{jet} is also directly proportional to the fuel loading, as shown in Table 1. Comparing the photos of the E21-6 and E21-3 flames, it can be seen that Re_{jet} also has an impact on flame length, with a noticeable increase in length when the Reynolds number is decreased from 6000 to 3000. Once again, it should be noted that the change in Re_{jet} is accompanied by a change in Φ_{jet}; in this case the two are inversely proportional. It can also be seen that the *n*-heptane and *n*-heptane/toluene flames have a longer flame length than the ethanol flame with the equivalent fuel and air flow rates (E21-5). Comparing them to the E21-3 flame, however, the flame lengths are approximately the same, and these flames all have approximately the same value of Φ_{jet}. These observations suggest that there is a relationship between flame length and Φ_{jet}, noting that the equivalence ratio is based on the central jet alone. It is therefore hypothesised that partial premixing between fuel and oxidant in the jet is of importance in these flames, as has been suggested in a previous study of dilute sprays carried by air [32].

3.2. Instantaneous OH-PLIF, UV-PLIF and Mie scattering signals

To analyse the flame structure in detail, imaging of OH-PLIF, UV-PLIF and droplet Mie scattering was performed at axial locations ranging from the jet exit plane to $x/D = 5.6$. Figure 3 displays selected instantaneous images and a superimposed image of the three different signals, for the E21-5 flame with the laser sheets centred at $x/D = 3.0$. These images were selected as they were deemed to be representative of the "typical" instantaneous signals obtained, and they display several key features of the flames studied. Also shown in the superimposed image is the overlap between the OH and UV signals (shown in dark blue), which was determined based on the product [OH]×[UV].

As suggested by the photographs in Figure 2, a double flame structure is evident from the OH-PLIF images, with two distinct OH layers on either side of the centreline, although the outer layer is significantly less intense (by a factor of approximately two). An additional region of OH can be seen on the inside, which corresponds to a separate reaction zone around an individual fuel droplet.

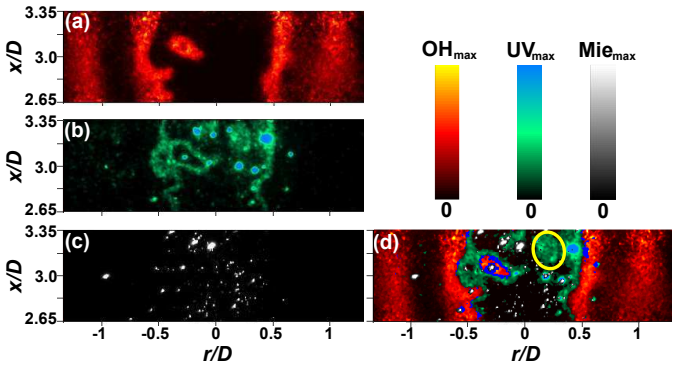

Figure 3: Selected instantaneous spatially and temporally matched images of (a) OH-PLIF, (b) UV-PLIF (CH_2O) and (c) Mie scattering, and (d) the three signals superimposed. Signal overlap ([OH]×[UV]) is shown in dark blue. Flame case E21-5, centred at $x/D = 3.0$.

The product [OH]×[UV] indicates that there is some overlap between OH and CH_2O in this region, which is indicative of local heat release [47]. The presence of an inner and outer flame front has been observed previously for similar flames [24, 26], where it is said to be caused by larger droplets being transported into the coflow, while smaller droplets (i.e. those with a small Stokes number) follow the flow field and move closer to the centreline. However, in a previous study with the same burner as that used in the current study, it was found that droplets tend to cluster near the pipe walls prior to exiting the jet [34]. This was attributed to the phenomena of Saffman lift and turbophoresis [48], which are associated with low Stokes number flow, suggesting that smaller droplets are more likely to be situated further from the centreline. Interestingly, while there is some evidence of fuel droplets penetrating the inner OH layer in Figure 3, the Mie scattering signal is low in this region—indicating that the droplets exist between the two flame fronts further upstream and have evaporated by $x/D = 3.0$. The distribution of droplets with respect to the two flame fronts is further explored in Section 3.4.

In Figure 3, the label of "UV" has been used to refer to the CH_2O-PLIF signal, as discussed in Section 2.2. The UV signal that lies just inside of the inner OH layer indicates the presence of intermediate species associated with

the preheat region—the same being true for the region enclosing the OH layer around the reacting droplet. In the region circled in Figure 3(d), an isolated region of UV-PLIF can be observed. Some high-intensity circular regions of UV-PLIF can also be seen in Figure 3, which at first glance appear to be related to interference caused by Mie scattering of the 355 nm light by droplets. However, further analysis of the UV images (for a range of axial locations and cases), in conjunction with the Mie scattering images from the 532 nm laser, indicates that interference from Mie scattering signal in the UV images is not significant. It is instead hypothesised that these high-intensity regions are related to pre-ignition reactions taking place around evaporating droplets; this is supported by the fact that these structures are observed more often in the regions corresponding to the formation of intermediate species.

To further illustrate the key features of these flames, Figure 4 shows an additional superimposed image, centred at $x/D = 1.5$, with labels to highlight particular aspects of the flame. Also included in Figure 4 is a post-processed version of the UV-PLIF image from the same instantaneous shot, where the continuous CH_2O structure on either side of the centreline has been isolated, as discussed in Section 2.2. This is particularly useful for analysing the spatial distribution of droplets, which is explored in Section 3.4.

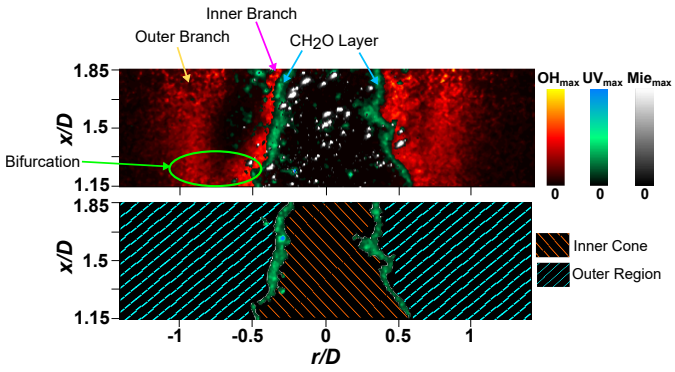

Figure 4: Instantaneous superimposed images OH-PLIF, UV-PLIF and Mie scattering, with key features as indicated. Flame case E21-5, centred at $x/D = 1.5$.

3.3. Instantaneous flame structure

To provide an insight into the near-field flame structure for the different cases, a series of superimposed images near the jet exit are shown in Figure 5. These images are centred at an axial location of approximately 7 mm above the jet exit ($x/D = 0.35$), such that the bottom of the laser sheet is aligned with the jet exit plane. It is evident from Figure 5 that all of the flames are attached, at least in terms of their outer flame front. The bifurcation of the flame into an inner and outer front can also be seen in some of the cases in Figure 5—this is most noticeable on the left-hand side of the E15-5 flame case. The CH_2O layer lies along the inside of this inner flame front (overlap is shown in blue), and in the cases where the "branching off" of the flame takes place, there appears to be no UV-PLIF signal corresponding to the outer branch. This can also be seen in Figures 3 and 4, where the UV-PLIF signal lies within the inside OH layer. This suggests that the inside flame front is the result of some of the fuel becoming prevaporised and mixing with the carrier air, since the concentration of CH_2O, and hence the UV-PLIF signal, is expected to be significantly higher under partially premixed conditions [49].

An interesting structure can be observed in the images in Figure 5(c), where there is no indication of an inner OH layer, yet the CH_2O layer appears to be branching away from the OH, as indicated by the lack of [OH]×[UV] signal in the upper regions of the images (particularly on the right-hand side of both images). This is indicative of pre-ignition reactions of the prevaporised fuel, leading to a lifted inner flame further downstream [32]. To further illustrate this, selected instantaneous UV- and OH-PLIF images for the H21-5 case, centred at $x/D = 0.75$, are shown in Figure 6.

Distinct ignition kernels can be observed in the OH signals in Figure 6; these are accompanied by the presence of CH_2O, which represents the preheat region prior to autoignition. It should be mentioned that due to the turbulent nature of the flames, out-of-plane effects could lead to apparent "discontinuities" in the OH sheet which are not actually present; however, there are several reasons why this is unlikely to be the case. First of all, these flames are dominated by stream-

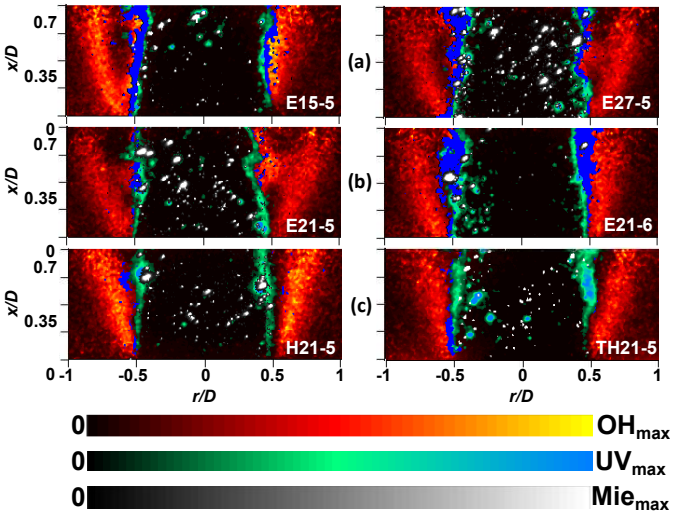

Figure 5: Superimposed signals from fuel droplets, OH and CH_2O for ethanol and n-heptane/toluene flames, centred at $x/D = 0.35$. Row (a) shows variation of fuel loading, row (b) shows variation of Re_{jet}, and row (c) shows the effect of toluene addition. [OH]×[UV] is included in dark blue.

ing flow in the axial direction, such that out-of-plane effects are not expected to be significant. If out-of-plane effects were responsible for the OH structures observed, then the CH_2O layer would be expected to show the same discontinuity, which is not the case. Additionally, the fact that the discontinuities are accompanied by CH_2O, and in some cases surrounded by it, further indicates that they are in fact ignition kernels, since this has been observed in previous studies involving autoignition and local extinction events [47, 15]. Finally, the discontinuities occur with much greater frequency for the n-heptane and n-heptane/toluene flames as opposed to the ethanol flames, and fuel type would not be expected to have a significant impact on out-of-plane effects. Therefore, it can be concluded that the isolated OH structures do indeed represent ignition kernels.

In each of the instantaneous images shown in Figure 6, the ignition kernels can be seen to form along the continuous CH_2O layer; more specifically, they tend to form on the outside of this layer—examples of this are labelled as A in

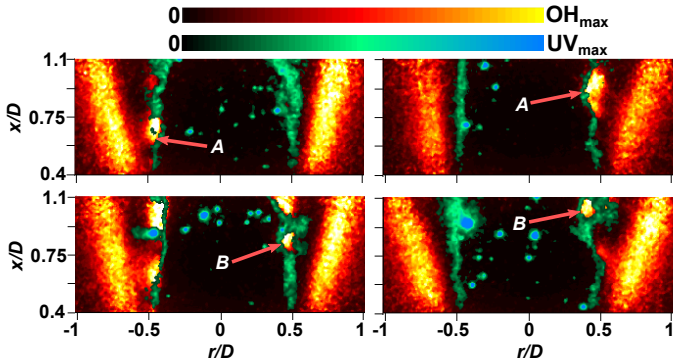

Figure 6: Selected instantaneous, superimposed images of OH- and UV-PLIF for the H21-5 flame, centred at $x/D = 0.75$.

Figure 6. Analysis of a series of images for this particular case revealed that when ignition kernels are detected (approximately 60% of images at $x/D = 0.75$), there is a 75% probability that they occur along the outside of the CH_2O layer, while the remaining 25% are enclosed within a layer of CH_2O (see the features labelled B in Figure 6). The fact that there is always UV-PLIF signal on the inside of the ignition kernels (in a radial sense) is an important observation, as it shows that the formation of intermediate species (including CH_2O) within the inner, partially premixed region is crucial to the formation of the inner flame structure.

The occurrence of ignition kernels at $x/D = 0.75$ was also detected for the n-heptane/toluene flames, while the ethanol flames did not show this feature consistently at this axial location. In the equivalent ethanol case (E21-5), the inner OH layer begins to form nearer to the jet exit, where bifurcations in the OH layer are more likely to occur, rather than isolated ignition kernels further downstream. In previous experiments using prevaporised fuels under similar conditions [50], an increase in lift-off height has been observed for n-heptane flames in comparison with ethanol. In the context of the current study, this suggests that the increased tendency for ethanol to ignite near the jet exit leads to the inner flame branching off from the stabilised, outer structure (i.e. a bifurcation), whereas for the n-heptane and n-heptane/toluene flames, distinct

ignition kernels are more likely to occur since the outer OH layer has greater separation further downstream. In addition, the lower boiling point and higher vapour pressure of ethanol (see Table 2) could also contribute to the inner flames stabilising nearer to the jet in these cases. A change in the autoignition process of ethanol droplets in comparison to n-heptane has been previously observed [51], where it was found that the lower volatility of n-heptane leads to the formation of flames around individual droplets. It is also worth mentioning that the stoichiometric mixture fraction is shifted toward the oxidant side (i.e. the coflow) for the n-heptane and n-heptane/toluene flames, which further separates the two structures. For the ethanol flames with greater values of Φ_{jet} (namely cases E21-3 and E27-5), there is an increased likelihood of ignition kernels being detected in the images centred at $x/D = 0.35$. While only a single case is shown in Figure 6, the Supplementary Material includes the statistical data relating to the detection of ignition kernels for the various cases, along with additional instantaneous images at $x/D = 0.35$. Intermittency plots of the OH signal are also included in the Supplementary Material, indicating a less stabilised inner structure in the near-field for the n-heptane and n-heptane/toluene flames—this is further explored in Section 3.6.

Figure 7 provides an overview of the flame structures from the jet exit up to $x/D = 5.3$, in the form of stacked, instantaneous, superimposed images, for the E21-5, E21-3 and H21-5 cases. Note that there are no images corresponding to the location $x/D = 2.25$ for the E21-3 and H21-5 cases in Figure 7. It should also be noted that the UV-PLIF signal has been removed from the n-heptane images for $x/D \gtrsim 2$, due to significant interference from LII resulting from the relatively high levels of soot in this region. The stacked images highlight the development of the inner and outer flame fronts and how this varies between the different cases. While the two flame fronts are clearly distinguishable in all cases, there is also significant interaction between them, particularly for the ethanol flames, where the inner and outer OH layers can be seen to form a single structure in some of the instantaneous images. This is a common occurrence in flames with multiple reaction zones [52], and is related to thermal "back-

support" between the two flame fronts, leading to a build-up of intermediate species and the merging of the two reaction zones in some instances. These images also show that the inner flame structure closes out nearer to the jet exit for the n-heptane case, despite initially forming further downstream. This is likely a consequence of increased premixing in the case of n-heptane due to the delayed ignition time.

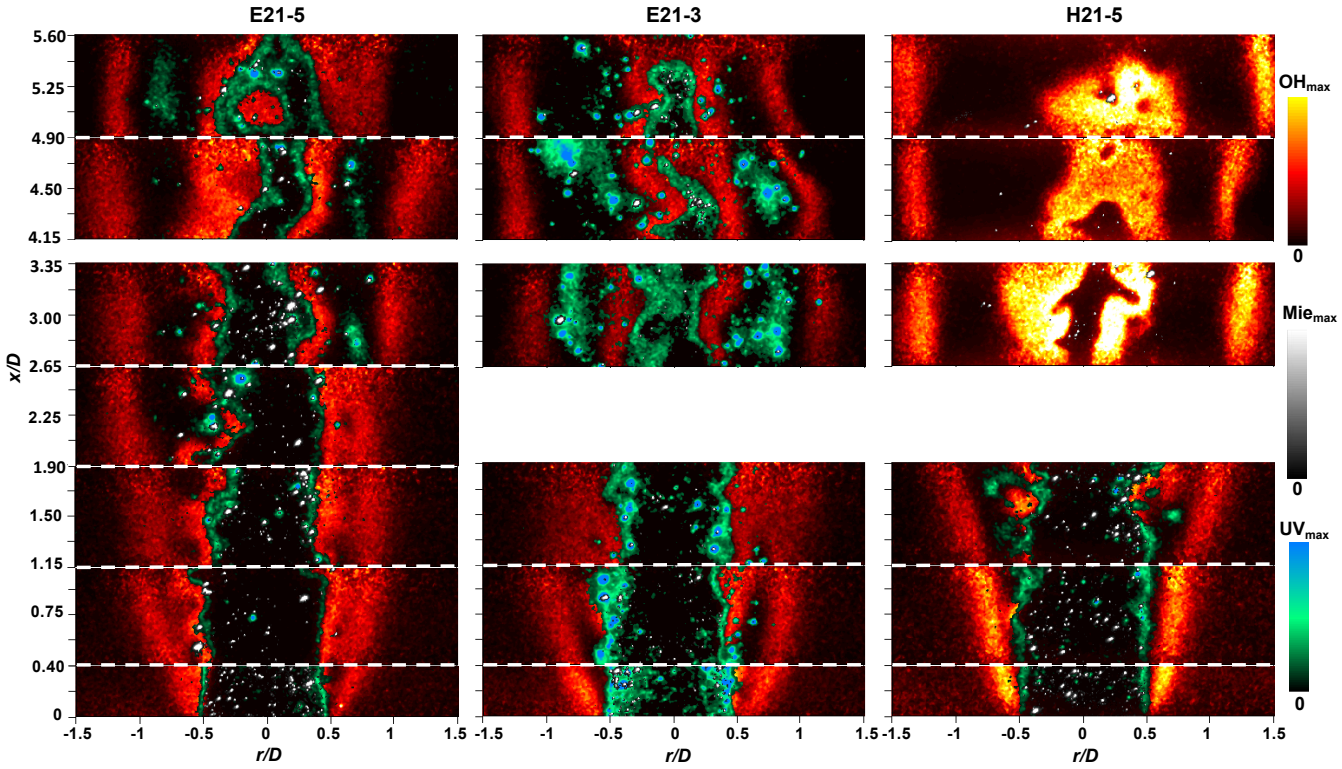

Figure 7: Stacked images at axial locations from the jet exit to $x/D = 5.6$, for flame cases E21-5, E21-3 and H21-5 (data were not collected for cases E21-3 and H21-5 at $x/D = 2.25$). Note: Images shown at different axial locations are not temporally matched.

Some droplets can be seen to penetrate the inner OH layer in Figure 7, although the majority are enclosed within the inner cone, particularly for the E21-5 case. It can also be seen that there are still liquid droplets present as the inner, partially premixed flame front begins to "close out" at $x/D \approx 5.6$. Additionally, some droplets can be seen to penetrate into the OH layer in this region.

It is worth noting that this closing out of the inner flame front corresponds to the tip of the blue inner cone, as seen in the photographs of the ethanol flames in Figure 2 (this is less clear in the n-heptane flame, due to increased luminosity from soot). In the photographs, a change in colour from a blue/violet shade to a yellow/orange in the inner region of the ethanol flames can be seen at the tip of the inner cone, which is attributed to the droplets penetrating into and through the tip of the inner flame front, where they evaporate and react as a diffusion flame, forming soot. Additionally, isolated regions of UV-PLIF are detected between the two flame fronts from $x/D \gtrsim 2.5$ (for the ethanol flames), which are associated with the onset of the sooting region that is characteristic of conventional diffusion flames [53]. This is particularly evident in the E21-3 images, where the UV-PLIF signal between the two flame fronts in the images centred at $x/D = 3.00$ and $x/D = 4.5$ is attributed to the presence of soot precursors (such as PAHs); this is consistent with the increased luminosity of this flame. It is worth noting here that the level of soot in the ethanol flames was below the LII detection threshold.

While only a limited set of results have been shown in this section, it was observed that the fuel loading and Reynolds number have a noticeable effect on the instantaneous flame structure. Specifically, the merging of the two flame fronts tends to become more frequent both at higher values of Re_{jet}, and lower values of $\dot{m}_f$—further evidence is included in the Supplementary Material, where additional instantaneous OH-PLIF images are shown for the different cases at a range of axial locations. The effect of Re_{jet} is expected, since the increased turbulence in the case of higher Re_{jet} promotes the transport of both heat and intermediate species between the two reaction zones. The trend observed with the change in fuel loading is attributed to a reduction in the number of droplets which penetrate the inner reaction zone, leading to a less pronounced double flame structure.

In the stacked images in Figure 7, the high-intensity circular regions in the UV signal are much more noticeable for the E21-3 case in comparison to the other cases shown. As mentioned in Section 3.2, these structures are attributed

to pre-ignition reactions around evaporating droplets. This suggests that there is increased evaporation of droplets in the near-field for the E21-3 case; this is further explored in the following section.

3.4. Droplet behaviour

To further investigate the distribution of droplets and how this relates to the overall flame structure, a useful measure is the droplet number count. Figure 8 displays the normalised droplet number counts with respect to axial location, with three separate plots to independently show the effects of variations in Reynolds number, fuel loading and fuel type. The number of droplets at each location was determined using a computational algorithm, based on the radially weighted Mie scattering signal over the height of the laser sheet and averaged over a set of 255 images for each case, as described in greater detail in Section 2.2. Also shown is the root-mean-square (RMS) values of the droplet counts, to provide an indication of the variability of the measurements. The mean and RMS plots were normalised against the maximum average droplet count from the E21-5 case, which is included in all plots as a reference case.

In Figure 8(a), a more gradual decay profile with increasing Re_{jet} is evident, with the E21-6 case ($Re_{jet} = 6000$) having the lowest droplet count in the near-field region, and the highest value further downstream at $x/D = 5.3$, compared to the $Re_{jet} = 5000$ and $Re_{jet} = 3000$ cases. Considering the difference in bulk flow rates, the greater average droplet number density near the jet exit for the case of lower Re_{jet} is expected. The difference in slopes between the three cases is a less obvious result, and indicates a significant increase in the evaporation of droplets in the near-field for the E21-3 case. This can be attributed to the droplets having greater momentum in the axial direction when Re_{jet} is higher, such that they tend to remain clustered towards the central axis, whereas there is an increased radial distribution of droplets towards the hot coflow when Re_{jet} is lower, leading to increased evaporation. This is supported by analysis of the Mie scattering images in terms of the signal intermittencies, which are included in the Supplementary Material and show an increased radial spread of droplets

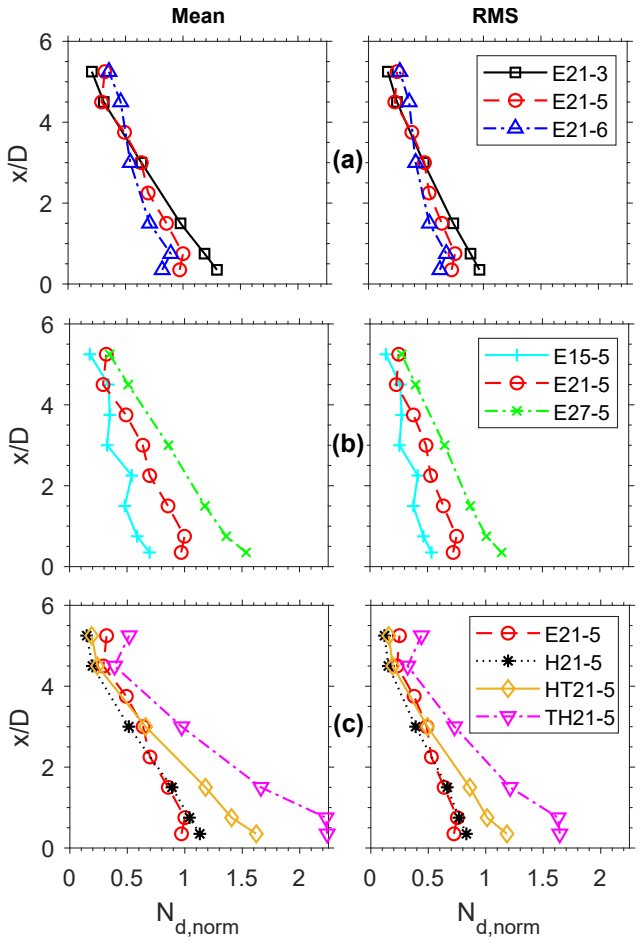

Figure 8: Radially-weighted axial profiles of mean droplet number counts with variations in (a) jet Reynolds number, (b) fuel loading and (c) fuel composition, normalised against the maximum droplet count from the E21-5 case.

when Re_{jet} is lower. This result is interesting, since an increase in turbulence could be expected to promote the radial transport of droplets towards the coflow, increasing the rate of evaporation. The fact that the opposite effect has been observed indicates that the magnitude of the turbulent fluctuations does not have a significant effect on the droplet dynamics, at least at the values of Re_{jet} used in this study.

As expected, Figure 8(b) shows that an increase in fuel loading leads to a general increase in the droplet count, although there are noticeable fluctuations with respect to axial location for the E15-5 case. Comparing (a) and (b) in Figure 8, and noting the fact that all of the plots are normalised against the E21-5 case, it is interesting to observe that cases E21-3 and E27-5 have very similar droplet counts, particularly in the near-field. Recalling the flame photographs, these two cases are very similar in terms of their visual appearance, which further highlights the influence of droplets in the near-field on the overall evolution of these flames, and also emphasises the need to be able to accurately predict droplet-combustion interactions in numerical modelling of spray flames.

The effect of fuel composition on the number of droplets is shown in Figure 8(c). There is a noticeable increase in the droplet number count as toluene is added to the fuel (HT21-5 and TH21-5 cases). This trend is likely a consequence of the lower volatility of toluene in comparison to ethanol and *n*-heptane. Specifically, toluene has a significantly lower vapour pressure and a higher boiling point (Table 2), thus a decreased rate of droplet evaporation for the *n*-heptane/toluene blends is expected. Furthermore, the fact that this increase in droplet count can be seen at the jet exit indicates that there is significant prevaporisation of the liquid droplets prior to exiting the jet.

As alluded to in Section 3.3, it is also of interest to investigate the radial location of droplets, particularly with regards to the penetration of droplets into the reaction zone. As discussed in Sections 2.2 and 3.2, the Mie scattering images were spatially filtered with respect to the UV-PLIF signal, to divide the droplets into those which occur within the "inner cone" and those which occur in the "outer region" (see Figure 4). These "inner" and "outer" droplet counts

are shown as ratios in Figure 9, focussing on the near-field region for variations in fuel loading.

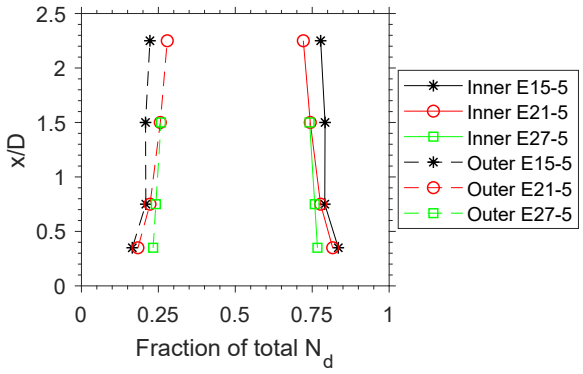

Figure 9: Proportion of droplets occurring inside and outside of the continuous CH_2O layer, for a range of fuel loadings and axial locations.

In Figure 9, it can be seen that droplets are consistently detected outside of the inner cone for all fuel loadings and axial locations shown. The proportion of droplets which exist outside of the inner cone (i.e. those labelled as "outer") ranges from approximately 15–25% of the total droplet count. Interestingly, the outer fraction can be seen to generally increase with distance from the jet exit for each of the cases. It should be mentioned that droplets which are outside of the inner cone would evaporate relatively quickly, due to the influence of both the hot coflow and the inner flame front. Therefore, the fact that the outer ratio increases suggests that droplets from the inner cone are consistently transported through the preheat region, and penetrate into the inner OH layer.

As mentioned in Section 3.3, the instantaneous images showed a higher degree of separation between the inner and outer flame structures with an increase in fuel loading. In previous experiments involving pressure-swirl atomised spray flames [24], the divergence between the inner and outer flame fronts was found to be related to the radial spreading of droplets, such that the outer flame is sustained by the vaporisation of larger droplets. Within the context of the droplet fractions displayed in Figure 9, in conjunction with the normalised number

counts shown in Figure 8(b), it can be seen that there is an increase in both the number and proportion of droplets which penetrate through the inner preheat layer for the E27-5 flame. Although there are key differences between the flames being studied here and those of Rodrigues et al. [24], the findings indicate that the radial distribution of droplets is a crucial factor leading to the development of a dual flame structure, in addition to the partial premixing of prevaporised fuel.

3.5. Mean flame structure: ethanol flames

To further investigate the flame structure and the effects of fuel loading and Reynolds number, radial plots of the time-averaged OH and UV signals at four different axial locations are shown in Figures 10 and 11. The laser sheets were centred at the axial heights stated in the figures, and the radial signals correspond to a horizontal line at these heights. The averaged OH and UV plots are respectively normalised against the maximum average OH and UV signal intensity from all cases involving ethanol flames; that is, the same normalising value has been used for the different cases shown in Figures 10 and 11. In addition to time averaging, the signals on either side of the centreline were also averaged to produce the plots.

The plots shown in Figures 10 and 11 display the OH and UV profiles side-by-side, noting that the OH profiles have been reflected about the vertical axis. From Figure 10, the mass loading of liquid fuel can be seen to have a noticeable impact, particularly in regards to the formation of a double flame structure. This is highlighted by the OH plots, which show two distinct peaks at all locations for the highest fuel loading case (E27-5), while the E15-5 signals only show a single peak. The intermediate case, E21-5, can also be seen to have a secondary peak, although it is much less defined than the E27-5 case. It should be mentioned that due to turbulent fluctuations in the flames, the averaging process leads to a "blurring" effect, such that some structures cannot be distinguished. At $x/D = 4.5$ (and to a lesser extent at $x/D = 3.0$) the OH signal for the E15-5 case displays a "shoulder" feature rather than a peak, indicating that there is

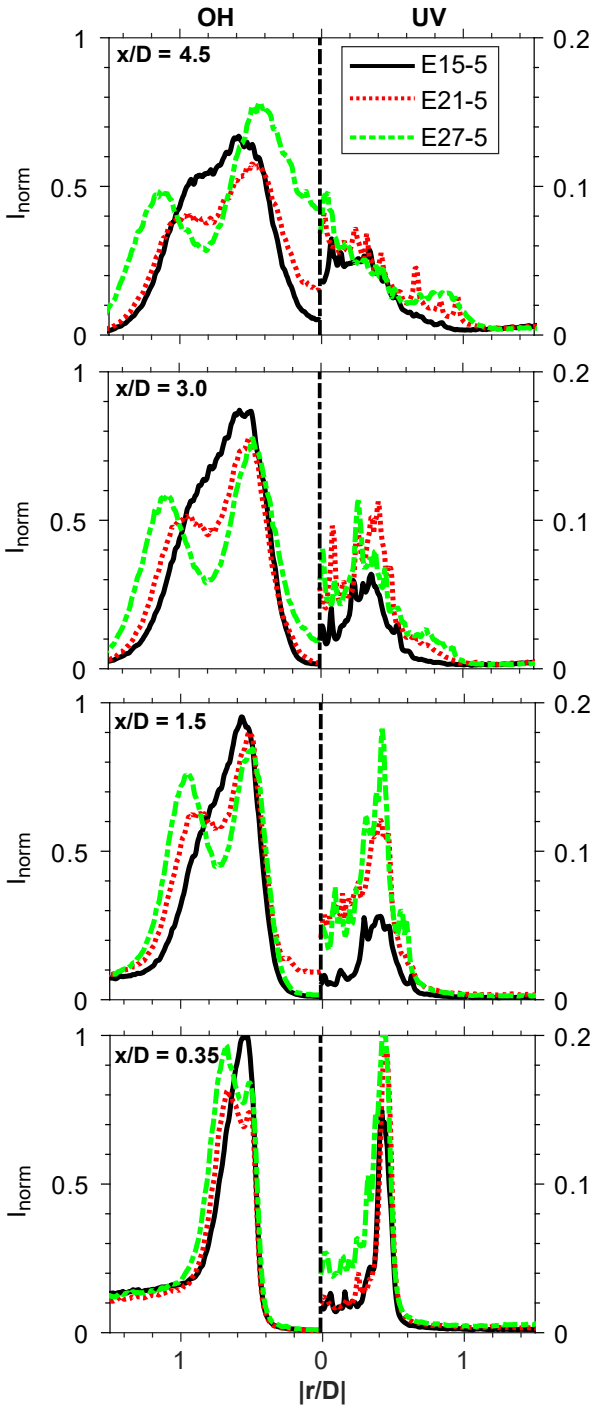

Figure 10: Radial profiles of normalised OH-PLIF (left) and UV-PLIF (right) signals, at a range of axial locations for ethanol flames with three different fuel loadings.

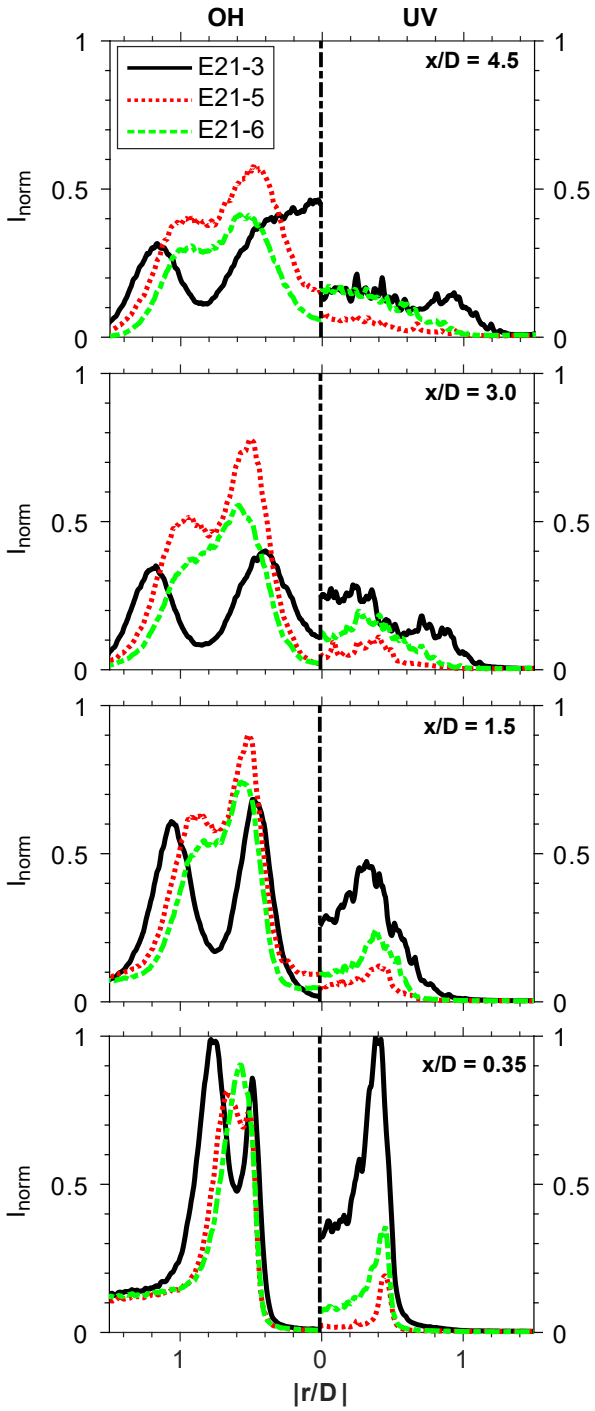

Figure 11: Radial profiles of normalised OH-PLIF (left) and UV-PLIF (right) signals, at a range of axial locations for ethanol flames with three different Reynolds numbers.

an inner and outer flame front present, but this double flame structure is less pronounced and is somewhat obscured by the averaging process. It can also be seen that the radial location of the OH peak in the E15-5 case approximately aligns with the inside peaks of the two higher fuel loading cases at the various heights, indicating that the inner flame front is more dominant when the fuel loading is lower. This is likely due to the reduced number of droplets penetrating the inner flame front and reacting with the hot coflow in the E15-5 flame, as shown by the droplet counts in Figure 9.

For all cases in Figure 10, the UV signal can be seen to reach its maximum within $r/D < 0.1$ at $x/D = 4.5$, representing the beginning of the tip of the inner flame. The UV plots show a similar shape for the three fuel loadings, with the magnitude generally showing an increase with increasing fuel loading, although this change is relatively small at most locations. The non-zero centreline UV signal near the jet exit is related to the isolated regions of UV-PLIF discussed in Section 3.2, and this appears to increase with fuel loading.

In Figure 11, Re_{jet} can also be seen to have a significant impact on the flame structure. Specifically, the double flame structure is much more pronounced for the $Re_{jet} = 3000$ case, with separate OH layers evident in the near-field. At $x/D = 4.5$, the inner OH layer can be seen to reach its maximum at the centreline for this case, representing the tip of the inner flame front at this axial location. In contrast, the inner peaks of the OH signals in the E21-5 and E21-6 cases at $x/D = 4.5$ occur at radial positions of approximately $r/D = 0.4$ and $r/D = 0.5$, respectively. This indicates that the inner flame front persists further downstream for the higher Re_{jet} cases.

It is interesting to note that the total flame length decreases with increasing Re_{jet} for these flames (see Figure 2), while the inner flame structure is shown to have the opposite relationship (Figure 11). When Re_{jet} is higher, the rate of evaporation in the jet increases, leading to an increased degree of premixing such that the flame favours the partially premixed mode (i.e. the inner cone). When Re_{jet} is lower, there is less partially premixed fuel to sustain the inner flame front downstream, with a greater number of droplets evaporating in the

presence of the hot coflow and reacting as a diffusion flame, hence a greater flame length. This also explains the decrease in flame luminosity as Re_{jet} is increased (Figure 2), since an increase in the degree of partial premixing generally suppresses soot formation, provided that Φ_{jet} is sufficiently low ($\lesssim 10$) [54, 55]. Previous numerical work has indicated that the formation of a double (or triple) flame structure is very sensitive to the evaporative time scale [28]. In the context of the current findings, this emphasises the importance of droplet evaporation and the near-field structure on the overall behaviour of the flame.

Another observation from Figure 11 is that the intermediate case with $Re_{jet} = 5000$ (E21-5) has the highest magnitude in terms of OH signal at all locations, except for $x/D = 0.35$, at which point it has the lowest signal. First of all, it should be noted that due to the qualitative nature of the results, it is difficult to directly compare signal magnitudes, because they could be affected by changes in signal quenching in the different flames. Nevertheless, this apparent non-monotonic behaviour with respect to Re_{jet} highlights the complex nature of turbulent and transitional spray flames, in terms of the competing effects of droplet residence time and mixing/evaporation processes. It can also be seen that this case has the lowest UV signal at all locations. The E21-3 case has a significantly higher UV signal, particularly near the jet exit, and the high magnitude at the centreline for this case is also worth noting. This would seem to indicate that interference from droplets is responsible (since the E21-3 case has a greater number of droplets in the near-field); however, if this were the case then the centreline signal would be expected to be higher for the E21-5 case compared with the E21-6 case (see Figure 9), while the opposite is true. Although this indicates that the change in UV signal intensity is not a direct result of interference from droplets, the signal magnitudes at the centreline suggest that it is also not solely a result of increased concentration of CH_2O in the preheat region. At this stage it is not possible to determine an exact cause, although the instantaneous images show that there is a greater proportion of high-intensity, circular structures in the UV-PLIF signal for the E21-3 and E21-6 cases, which, as discussed in Section 3.2, is indicative of pre-ignition reactions

surrounding droplets.

In the E21-3 case, peaks in the UV-PLIF signal can also be seen between the two OH layers (at $r/D \approx 0.8$) at the axial locations of $x/D = 4.5$ and $x/D = 3.0$. Referring back to Figure 10, this feature is also evident for the E27-5 flame (and to a lesser extent the E21-5 flame) at $x/D = 4.5$. These two cases (i.e. E27-5 and E21-3) also have the most pronounced double flame structure, as evidenced by the OH profiles. Referring again to the droplet plots (Figures 8 and 9), both of these cases have a relatively high number of droplets near the jet exit, with the majority having evaporated by $x/D = 4.5$. While the inner and outer droplet profiles are not included for the E21-3 case, Figure 9 shows that there is a significant number of droplets outside of the inner cone in the near-field for the E27-5 case, and it is reasonable to extend this reasoning to the E21-3 flame. Therefore, this secondary peak in the UV-PLIF signal is attributed to the increased proportion of droplets penetrating through the inner preheat region, and subsequently evaporating and reacting with the hot coflow as a diffusion flame. This is also consistent with the increased luminosity of these flames, and the change in colour at approximately $x/D = 4.5$, indicating the presence of nascent soot.

3.6. Effect of fuel type

To analyse the effect of toluene addition on flame structure in the near-field, shared radial plots of OH- and UV-PLIF for cases H21-5, HT21-5 and TH21-5 are shown in Figure 12, along with the E21-5 case for reference, from $x/D = 0.35$ to $x/D = 1.5$. Once again, the plotted data are averaged, normalised signals, using the maximum average intensity from the three axial locations as the normalising value. At the location nearest to the jet exit ($x/D = 0.35$), a single OH structure is evident in all of the n-heptane/toluene cases, which develops into a double flame structure with two distinguishable peaks further downstream. All three of the cases with n-heptane have very similar OH profiles, with the radial location of the peaks coinciding with each other at each of the heights, indicating that the addition of toluene does not significantly affect the

near-field flame structure. In saying this, the magnitude of the OH peaks can be seen to decrease with toluene addition, particularly for the outer peaks (when multiple peaks are present). Again referring to the droplet plots, this difference is attributed to the decreased rate of evaporation which occurs with toluene addition, which results in a lower concentration of radicals near the jet exit.

For the UV plots, the data have been omitted for $x/D = 1.5$, due to significant interference from LII, particularly in the cases containing toluene. The increased intensity of the UV-PLIF signal with addition of toluene is thus likely a result of increased levels of PAH when toluene is added, which is consistent with previous findings based on prevaporised n-heptane/toluene flames under similar conditions [23, 56]. It is interesting to note that the UV signal intensity for the two cases containing toluene is very similar at $x/D = 0.35$, despite the TH21-5 case having twice the concentration of toluene and a significantly higher intensity at $x/D = 0.75$. Previous results relating to prevaporised fuels indicate that as the proportion of toluene is increased, the concentration of PAH increases at all axial locations where PAH is present [56]. It is therefore hypothesised that the amount of vaporised toluene is approximately the same for both cases at $x/D = 0.35$, which is supported by the higher droplet count for the TH21-5 case (see Figure 8(c)).

It is interesting to note the difference in the OH profiles between the n-heptane/toluene cases and the ethanol case. For the ethanol flame, the inner peak can be seen to occur nearer to the jet exit, while it only becomes prominent at $x/D = 1.5$ for the other cases. At this location, the signal corresponding to the inner peak is considerably lower than the outer peak for the cases with n-heptane, while the opposite is true for the E21-5 case, along with the remainder of the ethanol flames (Figures 10 and 11). Interestingly, the instantaneous images show that the OH signal intensity is actually higher in the inner region for all cases—examples at $x/D = 1.5$ are included in the Supplementary Material. The reason that the averaged profiles show a greater outer peak for the n-heptane and n-heptane/toluene cases is that for these flames, the signal is less consistent in the near-field, suggesting a less stabilised inner flame structure,

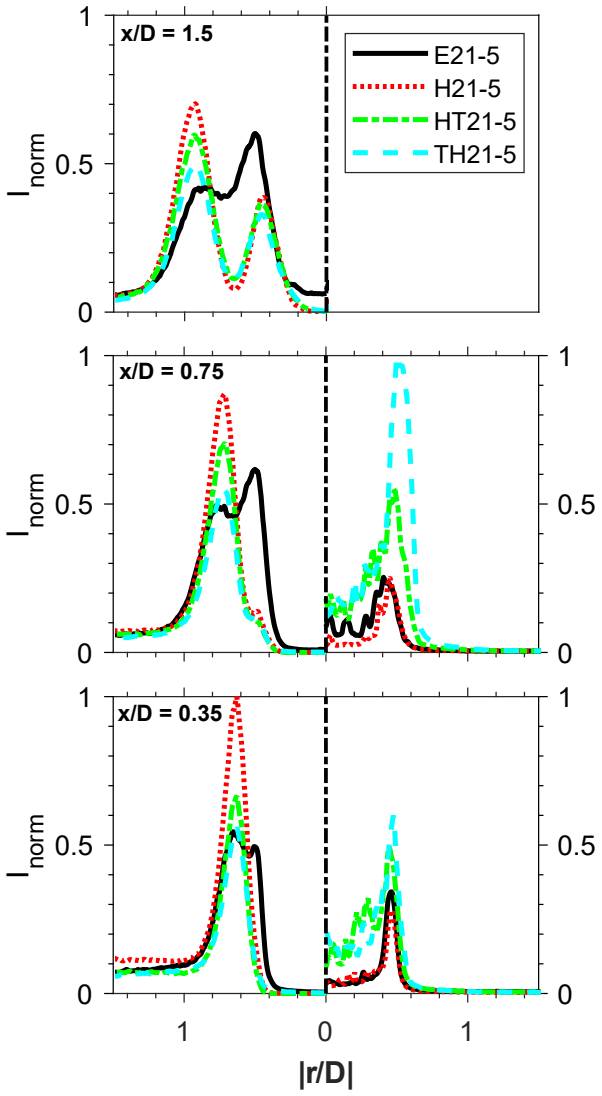

Figure 12: Radial profiles of OH and CH_2O in the near-field for flames of varying fuel composition.

which is supported by the OH intermittency images shown in the Supplementary Material.

To investigate the formation of soot and how it relates to the flame structure, radial profiles of the average soot volume fraction (f_v) at a range of axial locations are shown alongside normalised signals of OH-PLIF in Figure 13. In these plots, results correspond to the two n-heptane/toluene blends and the purely n-heptane case, at the three furthest-downstream axial locations. Note that none of the ethanol cases are included, since the level of soot in these flames was below the LII detection threshold.

A consistent increase in soot volume fraction with toluene addition is noticeable in Figure 13, with very low levels of soot detected for the n-heptane flame. This is due to the relatively high sooting propensity of toluene, as has been well-documented in the literature [23, 57]. For both the HT21-5 and TH21-5 cases, the LII signal can be seen to peak at approximately $r/D = 0.8$, which corresponds to the region between the two flame fronts, where the OH is at a minimum. There is a sharp drop in f_v for $r/D > 1$, corresponding to the outer peak in the OH signal, suggesting that the soot is oxidised by the outer flame front, noting that OH is known to oxidise soot [58]. It should be noted that much of the soot occurring between the two flame at the locations shown in Figure 13 is convected further downstream, where further mixing between soot and OH leads to oxidation of the soot [59].

4. Conclusions

The structure of dilute spray flames in a hot and low-oxygen environment has been studied using a combination of laser diagnostic techniques. Fuel composition, jet Reynolds number and fuel loading were independently varied, and a number of key findings were obtained:

- All flames exhibited a so-called "double-flame" structure to some extent, which is associated with prevaporisation of fuel, along with the penetration of droplets through the inner reaction zone.

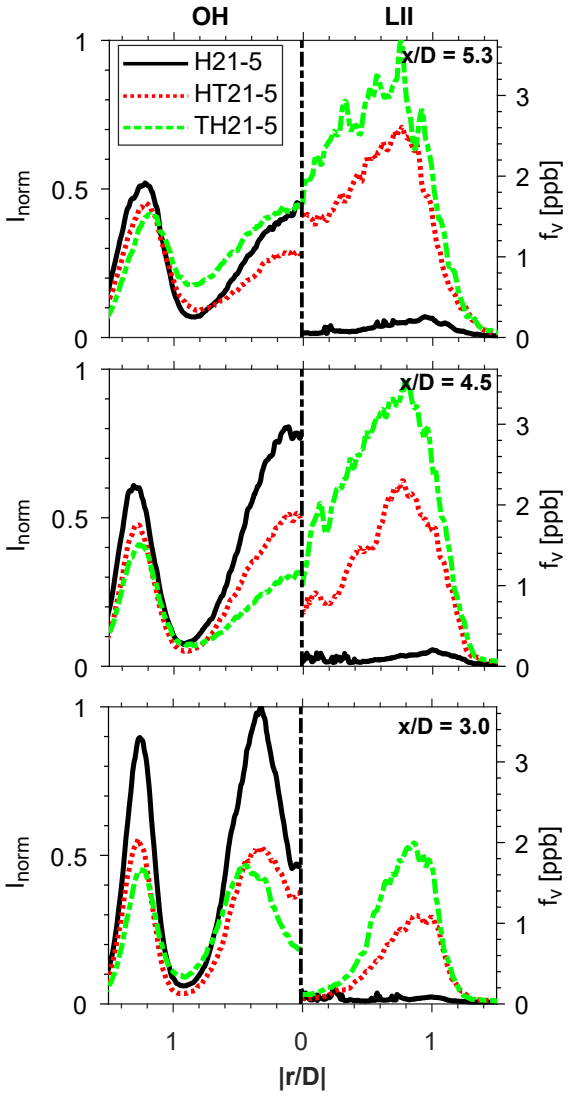

Figure 13: Radial profiles of OH-PLIF and f_v for the n-heptane flame (H21-5), and the 1:3 (HT21-5) and 1:1 (TH21-5) n-heptane/toluene flames from $x/D = 3.0$ to $x/D = 5.3$.

- The inner flame structure either "branches away" from the outer structure as a bifurcation, or undergoes a separate autoignition process, accompanied by distinct ignition kernels. It was found that ignition kernels are much more likely to occur for the n-heptane and n-heptane/toluene cases in comparison to the ethanol flame with equivalent fuel loading and Reynolds number. A reduction in Reynolds number and an increase in fuel loading also leads to an increased likelihood of kernel formation as opposed to bifurcations, which is related to an increased equivalence ratio in the jet.

- The distribution of droplets in the near-field was found to have a significant impact on the overall evolution of the flames. Analysis of the Mie scattering signals, in conjunction with simultaneous CH_2O imaging, revealed that droplets are consistently transported through the initial preheat region and into the inner OH structure, which plays an important role in the formation of a double flame structure.

- Analysis of the mean signals indicates that the double flame structure is more pronounced for lower Reynolds numbers and higher fuel loadings, with two distinct peaks in the OH signals evident in some instances.

- Toluene addition was found to have little effect on the overall flame structure, despite the increase in soot volume fraction. Combined analysis of the mean soot volume fraction and radial OH-PLIF signal indicates that soot is formed between the two flame fronts, and is oxidised in the outer reaction zone.

These findings provide a valuable insight into the underlying mechanisms which lead to the complex structures observed in spray flames in a hot and low-oxygen environment. While flames with similar structures have been studied previously, the parametric nature of this study—in terms of the independent variation of a range of jet boundary conditions—is an important distinction. This allows direct comparisons to be made between the various cases in order to better understand

the factors which influence the flame structure. This is particularly important, since it is difficult to predict the effect of such changes in boundary conditions in turbulent spray flames, due to the coupled interactions between turbulence, chemistry and droplet evaporation. Although primarily qualitative in nature, the results presented here are of particular importance for the prediction of bifurcating flame structures and the presence of ignition kernels under varying conditions. This is an important step towards the development of more efficient and robust numerical models of spray combustion, which will in turn enable improvements in the efficiency of practical combustion devices.

Acknowledgements

The authors would like to thank Dr Jingjing Ye for her contribution in the design of the burner used for these experiments, and Dr Thomas Kirch for his assistance with data collection. The support from the University of Adelaide is acknowledged, along with the financial support provided by the Australian Research Council (ARC) and the Future Fuels Cooperative Research Centre (CRC): Project RP1.10–04.

References

[1] P. Jenny, D. Roekaerts, N. Beishuizen, Modeling of Turbulent Dilute Spray Combustion, Prog. Energy Combust. Sci. 38 (2012) 846–887.

[2] G. M. Faeth, Current status of droplet and liquid combustion, Prog. Energy Combust. Sci. 3 (1977) 191–224.

[3] S. Hochgreb, Mind the gap: Turbulent combustion model validation and future needs, Proc. Combust. Inst. 37 (2019) 2091–2107.

[4] G. M. Faeth, Mixing, transport and combustion in sprays, Prog. Energy Combust. Sci. 13 (1987) 293–345.

[5] A. R. Masri, Turbulent Combustion of Sprays: From Dilute to Dense, Combust. Sci. Technol. 188 (2016) 1619–1639.

[6] R. Lebas, T. Menard, P. A. Beau, A. Berlemont, F. X. Demoulin, Numerical simulation of primary break-up and atomization: DNS and modelling study, Int. J. Multiphase Flow 35 (2009) 247–260.

[7] B. Merci, D. Roekaerts, A. Sadiki (Eds.), Experiments and Numerical Simulations of Diluted Spray Turbulent Combustion, Vol. 17 of ERCOFTAC Series, Springer Netherlands, Dordrecht, 2011.

[8] M. Zheng, G. T. Reader, J. Hawley, Diesel engine exhaust gas Recirculation—a review on advanced and novel concepts, Energy Convers. Manage. 45 (2004) 883–900.

[9] A. A. V. Perpignan, A. Gangoli Rao, D. J. E. M. Roekaerts, Flameless combustion and its potential towards gas turbines, Prog. Energy Combust. Sci. 69 (2018) 28–62.

[10] I. I. Enagi, K. A. Al-attab, Z. A. Zainal, Liquid Biofuels Utilization for Gas Turbines: A Review, Renewable Sustainable Energy Rev. 90 (2018) 43–55.

[11] V. Mahendra Reddy, S. Kumar, Development of high intensity low emission combustor for achieving flameless combustion of liquid fuels, Propulsion and Power Research 2 (2013) 139–147.

[12] N. Ladommatos, S. Abdelhalim, H. Zhao, The effects of exhaust gas recirculation on diesel combustion and emissions, Int. J. Engine Res. 1 (2000) 107–126.

[13] A. Cavaliere, M. de Joannon, Mild Combustion, Prog. Energy Combust. Sci. 30 (2004) 329–366.

[14] M. de Joannon, G. Langella, F. Beretta, A. Cavaliere, C. Noviello, Mild Combustion: Process Features and Technological Constrains, Combust. Sci. Technol. 153 (2000) 33–50.

[15] P. R. Medwell, P. A. Kalt, B. B. Dally, Simultaneous Imaging of OH, Formaldehyde, and Temperature of Turbulent Nonpremixed Jet Flames in a Heated and Diluted Coflow, Combust. Flame 148 (2007) 48–61.

[16] C. Galletti, A. Parente, L. Tognotti, Numerical and experimental investigation of a mild combustion burner, Combust. Flame 151 (2007) 649–664.

[17] P. R. Medwell, P. A. M. Kalt, B. B. Dally, Imaging of Diluted Turbulent Ethylene Flames Stabilized on a Jet in Hot Coflow (JHC) Burner, Combust. Flame 152 (2008) 100–113.

[18] B. B. Dally, A. N. Karpetis, R. S. Barlow, Structure of turbulent nonpremixed jet flames in a diluted hot coflow, Proc. Combust. Inst. 29 (2002) 1147–1154.

[19] R. Cabra, T. Myhrvold, J. Chen, R. Dibble, A. Karpetis, R. Barlow, Simultaneous laser raman-rayleigh-lif measurements and numerical modeling results of a lifted turbulent H2/N2 jet flame in a vitiated coflow, Proc. Combust. Inst. 29 (2002) 1881–1888.

[20] J. Sidey, E. Mastorakos, Visualization of MILD combustion from jets in cross-flow, Proc. Combust. Inst. 35 (2015) 3537–3545.

[21] C. M. Arndt, M. J. Papageorge, F. Fuest, J. A. Sutton, W. Meier, M. Aigner, The role of temperature, mixture fraction, and scalar dissipation rate on transient methane injection and auto-ignition in a jet in hot coflow burner, Combustion and Flame 167 (2016) 60–71.

[22] J. Ye, P. R. Medwell, K. Kleinheinz, M. J. Evans, B. B. Dally, H. G. Pitsch, Structural differences of ethanol and DME jet flames in a hot diluted coflow, Combust. Flame 192 (2018) 473–494.

[23] M. J. Evans, P. R. Medwell, Z. Sun, A. Chinnici, J. Ye, Q. N. Chan, B. B. Dally, Downstream evolution of n-heptane/toluene flames in hot and vitiated coflows, Combust. Flame 202 (2019) 78–89.

[24] H. C. Rodrigues, M. J. Tummers, E. H. van Veen, D. J. E. M. Roekaerts, Spray Flame Structure in Conventional and Hot-Diluted Combustion Regime, Combust. Flame 162 (2015) 759–773.

[25] G. Continillo, W. A. Sirignano, Counterflow spray combustion modeling, Combust. Flame 81 (1990) 325–340.

[26] F. Shum-Kivan, J. Marrero Santiago, A. Verdier, E. Riber, B. Renou, G. Cabot, B. Cuenot, Experimental and numerical analysis of a turbulent spray flame structure, Proc. Combust. Inst. 36 (2017) 2567–2575.

[27] S. K. Marley, E. J. Welle, K. M. Lyons, W. L. Roberts, Effects of leading edge entrainment on the double flame structure in lifted ethanol spray flames, Exp. Therm Fluid Sci. 29 (2004) 23–31.

[28] L. Ma, D. Roekaerts, Numerical study of the multi-flame structure in spray combustion, Proc. Combust. Inst. 36 (2017) 2603–2613.

[29] H. K. Motaalegh Mahalegi, A. Mardani, Investigation of fuel dilution in ethanol spray MILD combustion, Applied Thermal Engineering 159 (2019) 113898.

[30] J. D. Gounder, A. Kourmatzis, A. R. Masri, Turbulent piloted dilute spray flames: Flow fields and droplet dynamics, Combust. Flame 159 (2012) 3372–3397.

[31] W. O'Loughlin, A. R. Masri, A new burner for studying auto-ignition in turbulent dilute sprays, Combust. Flame 158 (2011) 1577–1590.

[32] W. O'Loughlin, A. R. Masri, The Structure of the Auto-Ignition Region of Turbulent Dilute Methanol Sprays Issuing in a Vitiated Co-Flow, Flow, Turbulence and Combustion 89 (2012) 13–35.

[33] A. R. Masri, J. D. Gounder, Turbulent Spray Flames of Acetone and Ethanol Approaching Extinction, Combust. Sci. Technol. 182 (2010) 702–715.

[34] M. J. Evans, D. P. Proud, P. R. Medwell, H. Pitsch, B. B. Dally, Highly radiating hydrogen flames: Effect of toluene concentration and phase, Proc. Combust. Inst. (In press).

[35] R. J. Lang, Ultrasonic Atomization of Liquids, The Journal of the Acoustical Society of America 34 (1962) 6–8.

[36] R. Rajan, A. B. Pandit, Correlations to predict droplet size in ultrasonic atomisation, Ultrasonics 39 (2001) 235–255.

[37] S. Kruse, J. Ye, Z. Sun, A. Attili, B. Dally, P. Medwell, H. Pitsch, Experimental Investigation of Soot Evolution in a Turbulent Non-Premixed Prevaporized Toluene Flame, Proc. Combust. Inst. 37 (2019) 849–857.

[38] M. J. Mussche, L. A. Verhoeye, Viscosity of ten binary and one ternary mixtures, Journal of Chemical & Engineering Data 20 (1975) 46–50.

[39] A. M. Velásquez, B. A. Hoyos, Viscosity of heptane-toluene mixtures. Comparison of molecular dynamics and group contribution methods, J. Mol. Model. 23 (2017) 58.

[40] P. O. Witze, S. Hochgreb, D. Kayes, H. A. Michelsen, C. R. Shaddix, Time-Resolved Laser-Induced Incandescence and Laser Elastic-Scattering Measurements in a Propane Diffusion Flame, Appl. Opt. 40 (2001) 2443–2452.

[41] N. H. Qamar, Z. T. Alwahabi, Q. N. Chan, G. J. Nathan, D. Roekaerts, K. D. King, Soot volume fraction in a piloted turbulent jet non-premixed flame of natural gas, Combust. Flame 156 (2009) 1339–1347.

[42] Q. N. Chan, P. R. Medwell, P. A. M. Kalt, Z. T. Alwahabi, B. B. Dally, G. J. Nathan, Simultaneous imaging of temperature and soot volume fraction, Proc. Combust. Inst. 33 (2011) 791–798.

[43] B. Axelsson, R. Collin, P.-E. Bengtsson, Laser-induced incandescence for soot particle size measurements in premixed flat flames, Appl. Opt. 39 (2000) 3683.

[44] Q. N. Chan, P. R. Medwell, G. J. Nathan, Algorithm for soot sheet quantification in a piloted turbulent jet non-premixed natural gas flame, Exp. Fluids 55 (2014) 1827.

[45] S. Kook, R. Zhang, Q. N. Chan, T. Aizawa, K. Kondo, L. M. Pickett, E. Cenker, G. Bruneaux, O. Andersson, J. Pagels, E. Z. Nordin, Automated Detection of Primary Particles from Transmission Electron Microscope (TEM) Images of Soot Aggregates in Diesel Engine Environments, SAE Int. J. Engines 9 (2015) 279–296.

[46] C. Wang, Q. N. Chan, R. Zhang, S. Kook, E. R. Hawkes, G. H. Yeoh, P. R. Medwell, Automated determination of size and morphology information from soot transmission electron microscope (TEM)-Generated images, J. Nanopart. Res. 18 (2016) 127.

[47] R. L. Gordon, A. R. Masri, E. Mastorakos, Heat release rate as represented by [OH] × [CH2O] and its role in autoignition, Combust. Theor. Model. 13 (4) (2009) 645–670. doi:10.1080/13647830902957200.

[48] T. C. W. Lau, G. J. Nathan, Influence of Stokes number on the velocity and concentration distributions in particle-laden jets, J. Fluid Mech. 757 (2014) 432–457.

[49] B. A. V. Bennett, C. S. McEnally, L. D. Pfefferle, M. D. Smooke, M. B. Colket, Computational and experimental study of axisymmetric coflow partially premixed Ethylene/Air flames, Combust. Flame 127 (2001) 2004–2022.

[50] J. Ye, P. R. Medwell, M. J. Evans, B. B. Dally, Characteristics of turbulent n-heptane jet flames in a hot and diluted coflow, Combust. Flame 183 (2017) 330–342.

[51] R. L. Gordon, E. Mastorakos, Autoignition of monodisperse biodiesel and diesel sprays in turbulent flows, Exp. Therm Fluid Sci. 43 (2012) 40–46.

[52] M. S. Mansour, I. Alkhesho, S. H. Chung, Stabilization and structure of n-heptane flame on CWJ-Spray burner with kHZ SPIV and OH-PLIF, Exp. Therm Fluid Sci. 73 (2016) 18–26.

[53] J. Du, R. L. Axelbaum, The effect of flame structure on soot-particle inception in diffusion flames, Combust. Flame 100 (1995) 367–375.

[54] G. De Falco, M. Sirignano, M. Commodo, L. Merotto, F. Migliorini, R. Dondè, S. De Iuliis, P. Minutolo, A. D'Anna, Experimental and numerical study of soot formation and evolution in co-flow laminar partially premixed flames, Fuel 220 (2018) 396–402.

[55] A. Mitrovic, T. W. Lee, Soot formation characteristics of laminar partially premixed flames, Combust. Flame 115 (1998) 437–442.

[56] S. Park, Y. Wang, S. H. Chung, S. M. Sarathy, Compositional effects on PAH and soot formation in counterflow diffusion flames of gasoline surrogate fuels, Combust. Flame 178 (2017) 46–60.

[57] A. E. Daca, Ö. L. Gülder, Soot formation characteristics of diffusion flames of methane doped with toluene and n-heptane at elevated pressures, Proc. Combust. Inst. 36 (2017) 737–744.

[58] M. Stöhr, K. P. Geigle, R. Hadef, I. Boxx, C. D. Carter, M. Grader, P. Gerlinger, Time-resolved study of transient soot formation in an aero-engine model combustor at elevated pressure, Proc. Combust. Inst. 37 (2019) 5421–5428.

[59] S.-Y. Lee, S. R. Turns, R. J. Santoro, Measurements of soot, OH, and PAH concentrations in turbulent ethylene/air jet flames, Combust. Flame 156 (2009) 2264–2275.